NANO LETTERS

Letter

pubs.acs.org/NanoLett

Tuning Phase Stability of Complex Oxide Nanocrystals via Conjugation

Ho-Hung Kuo,[†] Lei Chen,[‡] Yanzhou Ji,[‡] Heng-Jui Liu,[†] Long-Qing Chen,[‡] and Ying-Hao Chu*[,†,§]

[†]Department of Materials Science and Engineering, National Chiao Tung University, Hsinchu 30010, Taiwan

[‡]Department of Materials Science and Engineering, Pennsylvania State University, University Park, Pennsylvania 16802, United States

[§]Institute of Physics, Academia Sinica, Taipei 105, Taiwan

Supporting Information

ABSTRACT: Nanocrystals (NCs) attract tremendous research interests because of their unique properties to meet the demands of functionalities. To date, hybrid NCs with multiple components are developed to meet the rising demands that could be very difficult, or even impossible to be achieved by single-component NCs. Tuning properties by strain via conjugation could be an alternative solution. Strain engineering has been discovered and widely applied to many thin-film materials for tuning physical properties. Then, there is a further question to be addressed in this study: can we take the advantages we have learned in heteroepitaxy of thin films and transfer that into the NC conjugation? In order to demonstrate this possibility, we investigated NC conjugation of $BiFeO_3$ and $LaAlO_3$. We found that change in either $LaAlO_3$-NC or $BiFeO_3$-NC size would change the stability of rhombohedral-to-tetragonal phase transition. The present results show that strain engineering is possible to be realized in not only thin film but also NC conjugation. The same concept should be applicable to other complex oxide systems in order to broaden their practical applications for the rising demands of multifunctionalities.

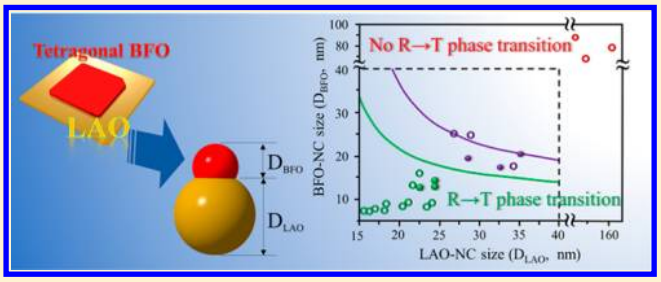

KEYWORDS: *Complex oxide, nanocrystal, heteroconjugation, strain engineering, $BiFeO_3$*

In order to tailor the unique properties of nanocrystals (NCs), the past decade has witnessed tremendous progress in the synthesis of NCs with controllable size, shape, and composition.[1,2] However, these NCs would unlikely meet the rising demands for the advanced breeds of building block for functional materials and devices.[3] Tuning properties via conjugation could be an alternative solution. For example, a demanding bandgap to a semiconductor device could be tuned via the conjugation of two materials with different bandgaps.[4] Also, the enhancement in photoluminescence of optical materials could be established by conjugating with noble metals.[5]

Complex oxide is a material that covers a broad spectrum of intriguing functionalities due to the interplays among degrees of freedom.[6,7] Recently, complex oxide NCs performed their remarkable optical, electronic, mechanical, thermal, magnetic, and quantum paraelectric properties.[8−10] Because of these properties, they are extensively exploited in technological applications like ferrofluid,[11] biomedicine,[12] and recording media.[13] For complex oxide thin films, the heteroepitaxy provides a powerful route to manipulate their lattice,[14] charge,[15] orbit,[16] and spin[17] degrees of freedom to enhance the functionalities. The key ingredient to drive these intriguing phenomena is the strain engineering, which is dominated by the epitaxial strain at the interface between the film and the substrate due to the difference in their lattice parameters. However, such a concept has not yet been applied to or found in complex oxide NC conjugation. Tuning properties of NCs via strain engineering could be traced back to Stranski−Krastanove (S-K) growth in 1938, known as "layer-plus-island growth".[18] S-K growth was the first mechanism about the formation of NC (island) on film that resulted from the mismatch-induced stress, reported by Ivan Stranski and Lyubomir Krastanov. When the deposited film is thinner than the critical thickness, the layer/substrate mismatch stress can drive the continuous growth of local nucleation and coalescence of adsorbate atoms into islands. This is the primary mode of applying stress to transform the two-dimensional (2D) thin film into 0D nanocrystal. Afterward, many exciting examples were studied to demonstrate the application of internal stress enhancing the properties of nanomaterials.[19,20] Continuously developing the idea of coupling internal stress and properties, the further concept of applying epitaxial strain to enhance the properties was proposed, known as strain engineering. For many materials, especially for complex oxides, their properties can be effectively tuned via this mechanism. The key question to be addressed in this study is the following: can we take the advantages we have learned in heteroepitaxy of thin film and transfer that into the NC conjugation? In the

Received: February 26, 2014
Revised: May 19, 2014
Published: May 28, 2014

   dx.doi.org/10.1021/nl500744h | *Nano Lett.* 2014, 14, 3314−3320

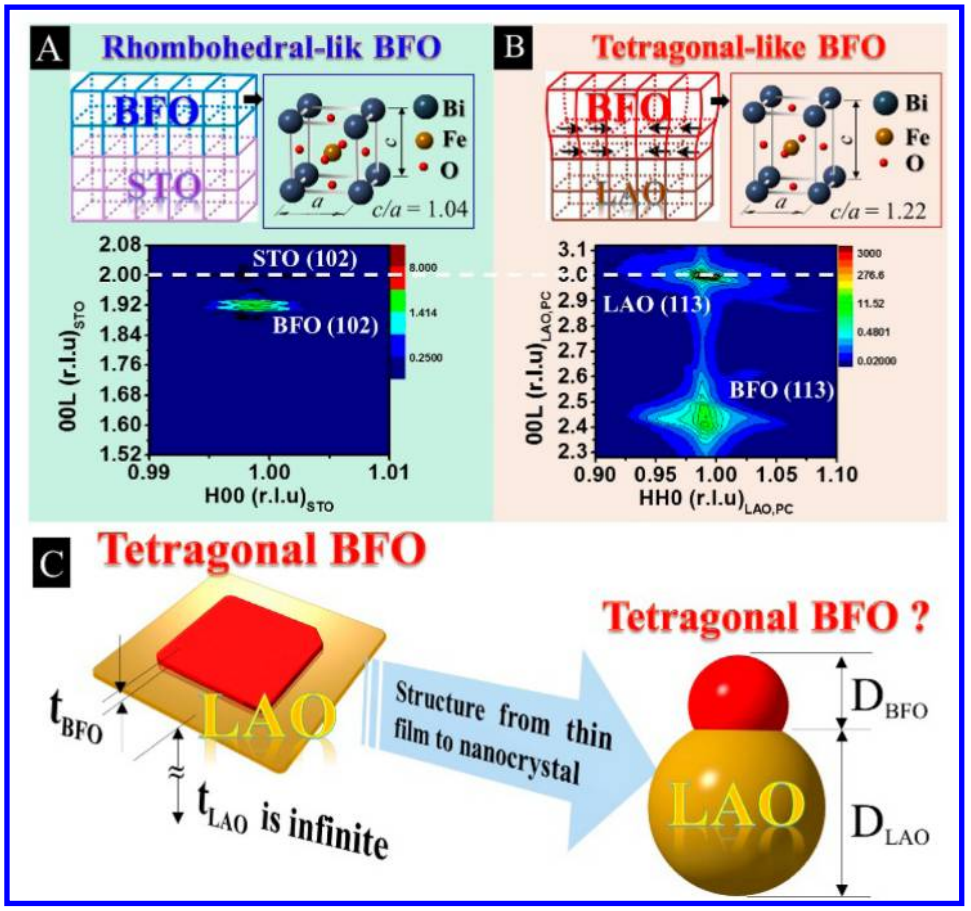

Figure 1. RSM results show BFO film of 20 nm epitaxially deposited on STO ($a \approx 3.905$ Å) and LAO ($a \approx 3.787$ Å) exhibits (A) R-phase ($a \approx b \approx 3.912$ Å, $c \approx 4.07$ Å, $c/a = 1.04$) by very small epitaxial strain and (B) T-phase ($a \approx 3.81$ Å, $b \approx 3.76$ Å, and $c \approx 4.656$ Å, $c/a = 1.22$) by a compressive strain about 4%, as described by the above illustration, respectively. (C) The idea of the present work is when the conjugation of BFO/LAO is transformed from 2D thin film to 0D NC, is it still possible to drive R → T phase transition in BFO-NC by the strain from the LAO-NC confinement? How the change in NC size influences the phase stability of BFO-NC?.

present work, we chose $BiFeO_3$ (BFO) as a model system to seek out this possibility.

BFO is one of the most important multiferroics at room temperature, that is, an oxide exhibits ferroelectricity and antiferromagnetism simultaneously at room temperature.[21] The ground state of BFO is a rhombohedrally distorted perovskite ($R3c$) with a lattice parameter of $a \approx 3.965$ Å, as abbreviated as R-phase. The phase stability of R-phase BFO can be tuned if an appropriate external constraint is imposed to it via epitaxial strain.[22−24] For example, when an epitaxial strain applied to BFO reaches a critical value (4−5%) by confinement of $LaAlO_3$ (LAO) substrate, BFO can transform from rhombohedral to tetragonal phase. These strain-driven phases with different crystal structures show different physical properties[24−27] from the parent phase. From these results, one can find a strong coupling between phase stability and properties of BFO thin film. However, such an interesting feature found in thin film is not yet demonstrated in free-standing NC. Therefore, we want to demonstrate tuning the phase stability of BFO via conjugation in order to deliver a concept that properties of complex oxide could be tuned not only in thin film but also in NC conjugation. The direct logic to the following experimental and simulation work will be the following:

1. Demonstration of applying epitaxial strain for tuning BFO phase stability via BFO/LAO heteroconjugation from which to deliver the concept of present work.

2. To demonstrate that synthesis of pure BFO-NC using pulsed laser ablation of BFO target in an appropriate solution is possible.

3. To demonstrate the possibility of tuning BFO phase stability via BFO-NC/LAO-NC heteroconjugation.

4. To illustrate the boundaries for NC size effect of BFO and LAO on BFO phase stability by simulation work and check it by experimental data.

Figure 1 shows the demonstration of tuning BFO phase stability in 2D thin film via epitaxial strain and the concept of present work. Epitaxial BFO films were prepared using pulsed laser deposition on LAO and $SrTiO_3$ (STO) substrates at substrate temperature of 700 °C with oxygen pressure of 100 mTorr. The growth rate was kept at 3 nm/min. The final BFO thickness was controlled by a combination of reflection high-energy electron diffraction (RHEED) and deposition time. Following growth, the films were cooled at oxygen pressure of 760 Torr to room temperature. The phase identification of BFO films with thickness of 20 nm on perovskite STO ($a \approx 3.905$ Å) and LAO ($a \approx 3.787$ Å) substrates were carried out using X-ray diffraction (XRD) reciprocal space map (RSM), as shown in Figure 1 panels A and B, respectively. The white dashed line marks the STO (102) peak and LAO (113) peak in RSMs. Since BFO (102) peak vertically aligned to STO (102) peak, as well as BFO (113) aligned to LAO (113), the BFO films on STO and LAO are both fully strained by their

dx.doi.org/10.1021/nl500744h | Nano Lett. 2014, 14, 3314−3320

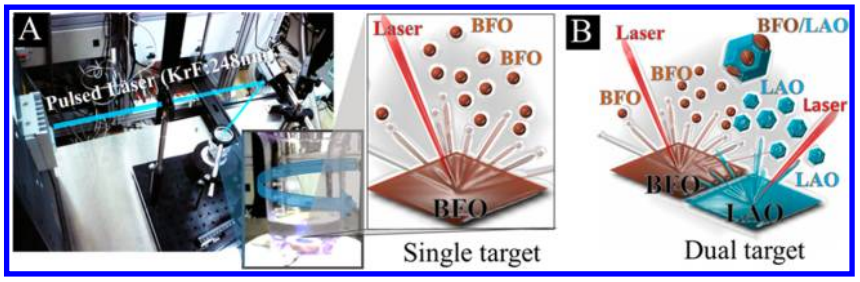

Figure 2. (A) Photo of PLA in liquids. KrF laser (248 nm) penetrates the liquid to bombard the target in a rotating beaker, and the schematic of BFO-NC fabricated from BFO single target into liquid. (B) Schematic of PLA of dual target (BFO and LAO) in liquid of rotating beaker in order to fabricate the conjugation of BFO-NC and LAO-NC.

substrates. Owing to the relatively large strain, BFO (113) peak in Figure 1B exhibits a much larger split than BFO (102) peak in Figure 1A. This result gives the important information that BFO structure has been elongated along *c*-axis due to compressive strain from LAO confinement, as indicated by the black arrows in the above illustration. Consequently, the BFO film on STO exhibits a rhombohedral-like phase (R-phase, $a \approx b \approx 3.912$ Å, $c \approx 4.07$ Å, $c/a = 1.04$); however, the one on LAO exhibits tetragonal-like phase (T-phase, $a \approx 3.81$ Å, $b \approx 3.76$ Å, and $c \approx 4.656$ Å, $c/a = 1.22$). In other words, because STO lattice parameter is very close to BFO, the epitaxial strain between them is too small to drive R → T phase transition and BFO still remains in R-phase. When BFO film is confined on the LAO substrate with relatively small lattice parameter, an epitaxial strain (>4%) is large enough to drive the phase transition. Nevertheless, we also found in our previous work that R → T phase transition will not happen if BFO film thickness is larger than 50 nm.[28] It could be interpreted by the formation of interfacial defect to relax the strain.

Then, an open question comes out in Figure 1C: what if the heteroepitaxy of tetragonal-like BFO on LAO transfers from thin film to NC? Is the T-phase still remaining in the BFO-NC? The epitaxial strain relaxation is exclusively related to film thickness (BFO thickness, t_{BFO}), while the substrate thickness (LAO thickness, t_{LAO}) is theoretically regarded as infinite. However, for the NC case both NC sizes of the heteroconjugation structure are supposed to affect the epitaxial strain relaxation. Another key question followed by this suggestion is how to define the size ranges of BFO-NC and LAO-NC, that is, D_{BFO} and D_{LAO}, which are able to induce a sufficient strain for R → T phase transition. In order to demonstrate this concept, the experimental and simulation works on the conjugation of BFO/LAO NC have been conducted as follows.

Figure 2 shows a photo of pulsed laser ablation (PLA) liquids and schematics of BFO-NC and conjugation of BFO/LAO NC by this process. The liquid is the mixture of distilled water and ethylene glycol in a rotating beaker. After focused by the lens, the KrF laser (λ = 248 nm, 10 Hz, 250 mJ/pulse) penetrates the liquid to bombard the BFO single target in order to synthesize BFO-NC into liquid, as shown in the schematics of Figure 2A. These pure BFO-NCs have been systematically identified using XRD, Raman spectrometery (Raman), X-ray absorption spectrometery (XAS), and electron energy loss spectrometery (EELS). These data are discussed in detail in the Supporting Information (Figure S1 and S2) from which one can realize that pure BFO-NC can be synthesized by this process at room temperature. The heteroconjugation NCs of BFO/LAO were fabricated by PLA of dual target in liquid, as shown in Figure 2B. Consequently, BFO-NC and LAO-NC can be conjugated with each other in the liquid, where the brown spheres represent BFO-NCs and the blue polyhedrons for LAO-NCs. Because NCs were fabricated into liquid by ablation of high-energy laser, the size range is from about 10 to 200 nm. These NCs were dropped on a carbon-coated Cu grid and investigated by high-resolution transmission electron microscopy (TEM) equipped with energy dispersive spectroscopy (EDS). The following JEOL microscopes operating at 200 kV were used: JEM-2010 with a LaB_6 thermo-gun and JEM-2100F with a field emission gun. The EDS was used to semi-quantitatively identify the elemental concentrations. Gatan commercial software (DigitalMicrograph 3.6.4) was conducted to run image processing of HRTEM image, including fast Fourier transformation (FFT) to get diffraction pattern and revised FFT for obtaining image with lower background noise. These data are discussed from Figures 3 to 5.

Microstructural and elemental examinations of BFO and BFO/LAO NCs are shown in Figure 3 panels A and B, respectively. According to Wulff construction theory, the

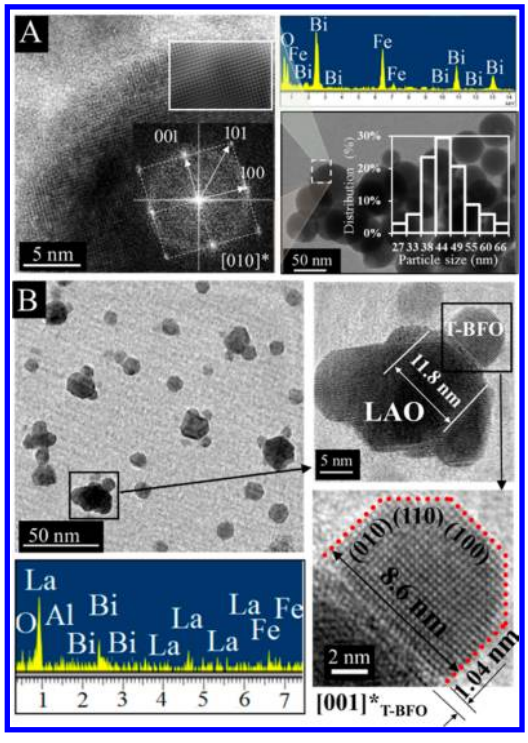

Figure 3. TEM and EDS examinations of (A) BFO-NCs, and (B) heteroconjugation NCs of BFO/LAO using pulsed laser ablation in the solution of ethylene glycol diluted by 50% distilled water.

dx.doi.org/10.1021/nl500744h | *Nano Lett.* 2014, 14, 3314−3320

difference in facet energy dominates the NC morphology. At the early stage of NC growth, the close-packed facets remain because they have the lowest energy and growth rate. Such a growth behavior results in a polygonal NC, especially for cubic materials. For 2D TEM images viewing from different directions, it is possible to see a polygonal NC revealing different morphology, as well as the BFO-NCs and LAO-NCs with size smaller than 15−20 nm in Figure 3B. With increasing size, the NC morphology becomes spherical in order to reduce the surface energy, just like the BFO-NCs with size larger than 25−30 nm, as shown in Figure 3A. Therefore, the NC morphology is dominated by its size based on Wulff construction.

The low-magnification TEM image in Figure 3A shows that BFO-NCs essentially have spherical morphology when their size is larger than 20 nm, as seen in the size distribution (27−66 nm). This is due to that the viscosity of solution has been enhanced by adding ethylene glycol, driving a cluster of randomly distributed atoms to shrink or condense into a spherical NC. EDS spectra including Bi, Fe, O were acquired overall from these spherical NCs and their elemental concentration ratio in atomic percent is semiquantitatively measured as Bi/Fe/O = 1:1:3. A systematic analysis of these BFO-NCs using XRD, Raman, XAS, and EELS are discussed in the supporting material. An individual BFO-NC was further investigated using high-resolution TEM (HRTEM), which is capable of proving lattice image of single crystal structure, as enlarged from the local area of the NC. The lattice image includes periodic fringes corresponding to the lattice planes. Using image processing, that is, FFT, these periodic fringes in real space can be transformed into diffraction spots in reciprocal space, as shown in the inset image of diffraction pattern. The incident beam of diffraction pattern is parallel to the [010] direction of rhombohedrally distorted pervoskite structure (R-phase, a = 3.96 Å, α = 89.5°), and the diffraction spots are corresponding to the (100), (001), and (101) facets of this structure, respectively.

HRTEM image and corresponding EDS spectra of conjugation NC of BFO/LAO are shown in Figure 3B. After identifying the lattice images of these hybrids, we know that the polygonal NCs are LAOs, and the smaller NCs grown on LAOs are BFOs. EDS spectra of La, Al, Bi, Fe, and O elements are contributed by the sum of these hybrids. It can be interpreted that due to the quenching effect and confinement of liquid, BFO, and LAO species nucleate and grow into NC very fast. However, owing to their different physical properties, such as melting point, the LAO-NC attempts to nucleate and grow earlier and faster than BFO-NC. Therefore, the following BFO species have the opportunity to nucleate on LAO facets to form hybrid structure. Enlarging one of BFO/LAO-NCs in the black frame, the lattice image reveals that BFO-NC the size of 8.6 nm is coherently conjugated with a LAO-NC facet the size of 11.8 nm. The width of coherent interface was measured to be 1.04 nm, containing several unit cells. The lattice image taken along with [001] direction of tetragonal-like BFO phase (T-phase, a = 3.68 Å, c = 4.66 Å) are composed of interference fringes belonging to the (100), (010), and (110) facets, as described by the red-dotted line. The lattice spacing of them was measured to be 3.68, 3.66, and 2.58 Å, respectively. These examinations clearly indicate that BFO-NC transformed from R-phase to T-phase only if an appropriate constraint is applied on it via conjugating with LAO-NC. Meanwhile, LAO-NCs with different sizes in BFO/LAO hybrids have been examined by HRTEM, which showed that the lattice constant of LAO does not change with increasing size. Instead, the BFO lattice constant changes due to the LAO conjugation. In this case, it could be considered that the NC size is the control parameter for phase transition of BFO/LAO hybrid.

The heterostructural NCs of BFO/LAO have been investigated in more detail using HRTEM. Two typical hybrid NCs of tetragonal-like BFO/LAO (T-BFO/LAO) were identified and discussed in Figures 4 and 5, respectively. The

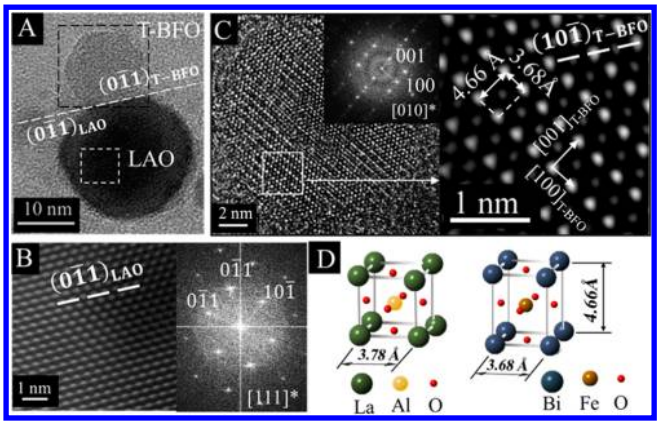

Figure 4. (A) TEM image showing the heteroconjugation of tetragonal-like BFO/perovskite LAO (T-BFO/LAO) and HRTEM images of (B) LAO-NC and (C) T-BFO NC. The pseudocubic models of LAO and T-BFO are shown in (D).

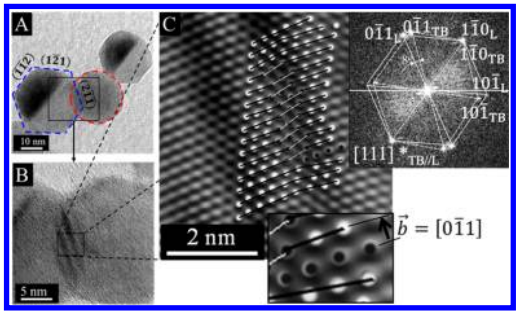

Figure 5. (A) TEM image showing a conjugation of three NCs, in which the spherical BFO at the middle conjugating with polygonal LAO-NCs on two sides, (B) HRTEM image taken along with the $[111]_{TB}//[111]_{L}$ direction of T-BFO and LAO showing the interface containing stacking faults, and (C) enlarged HRTEM image showing an interfacial dislocation with a Burger's vector of $[0\bar{1}1]$ resulted from the stacking faults in more than 10 atomic layers.

category we considered is the effect of BFO-NC and LAO-NC size on strain relaxation. When the BFO-NC is fully strained by LAO-NC with suitable size, as shown in Figure 4, the strain from LAO-NC confinement drives the phase transition of BFO-NC. The interfacial defects might be introduced to release the strain as the NC size is increased. The only proof to the strain relaxation in NC is to find the interfacial defects at heteroconjugated interface, as shown in Figure 5. This concept has been widely provided for the evidence of eliminating epitaxial strain in thin film case.

The first type of hybrid T-BFO/LAO is revealed in the TEM images of Figure 4A. It is showing a T-BFO of 12.8 nm coherently conjugated with a perovskite LAO of 21.9 nm. The coherent interface of T-BFO/LAO was identified to be $(\bar{1}01)_{T\text{-}BFO}//(0\bar{1}1)_{LAO}$. One can find the HRTEM image of

dx.doi.org/10.1021/nl500744h | Nano Lett. 2014, 14, 3314−3320

this coherent interface in the Supporting Information (Figure S3). The lattice image and corresponding diffraction pattern taken along with direction [111] of perovskite LAO-NC is shown in Figure 4B. The lattice spacing of $(0\bar{1}1)_{LAO}$ is measured to be 2.68 Å. In the diffraction pattern, Miller's indices of all diffraction spots are provided. These diffraction spots are contributed by the lattice planes of LAO structure, whose atomic model is given in Figure 4D. Figure 4C shows the lattice images and corresponding diffraction pattern taken along with direction [010] of T-BFO structure, whose atomic model is shown in Figure 4D as well. From the image, the lattice spacing of (001) and (100) was measured to be 4.66 and 3.68 Å, respectively. The c/a ratio was calculated to be 1.26, approximately the value we measured in Figure 1 for R → T phase transition of BFO thin film by epitaxial confinement of LAO substrate. Back to Figure 3, the lattice spacing of $(\bar{1}01)_{R\text{-}BFO}$ in rhomohedral BFO-NC (R-BFO) is measured to be 2.8 Å, which is larger than 2.68 Å of $(0\bar{1}1)_{LAO}$ in perovskite LAO. Owing to the difference between lattice spacings, 4.47% of compressive strain is induced at the interface between R-BFO and LAO NCs. Such a strain is capable of driving R → T phase transition in BFO-NC. This result is in a good agreement with the case of BFO thin film reported by Zeches et al.[22] They also found that the out-of-plane lattice parameter (c along z-axis) changes from 4.06 Å in the R-BFO to 4.65 Å in the T-BFO when the BFO thin film was epitaxially deposited on a perovskite LAO (a = 3.79 Å) substrate. Meanwhile, the in-plane lattice parameter (either a component along x-axis or b component along y-axis) is constrained by the substrate and changed slightly from ~3.8 Å in the R-BFO to ~3.7 Å in the T-BFO. The c/a ratio then can be changed from 1.07 in R-BFO to 1.27 in T-BFO.

The lattice images and corresponding diffraction pattern of the other type of T-BFO/LAO is shown in Figure 5. The conjugation of three NCs has been investigated by TEM, as shown in Figure 5A. It can be seen that the middle one has spherical shape, and the NCs on two sides are in polygonal shape. These two polygonal NCs both exhibit two facets with different contrast. When the facet normal has larger angle-to-electron beam, the facet image is revealed in stronger contrast. To enlarge the interface between left and middle NC, an interfacial lattice image was acquired and shown in Figure 5B. The diffraction pattern taken from the lattice image of Figure 5B by FFT processing and enlarged image of interface is shown in Figure 5C. According to the identification via measuring the lattice spacings and angles of lattice planes in diffraction pattern, it gives the information that the NC described by red-dotted line is T-BFO (20.3 nm) conjugated with perovskite LAO-NC (26.8 nm) by the blue-dotted line. Their crystal facets contributed diffraction spots to the pattern, as denoted by TB and L, respectively. The zone axis of diffraction pattern is parallel to $[111]_{TB}//[111]_{L}$ direction of T-BFO and LAO-NC. The facets of LAO-NC at left were identified as $\{2\bar{1}\bar{1}\}_{L}$ group in Figure 5A. The T-BFO is conjugated on $(2\bar{1}\bar{1})_{L}$ of LAO-NC, and its size is obviously larger than the facet width. Accordingly, interfacial defects are supposed to be introduced in order to accommodate the interfacial strain, as well as three parallel Moiré fringes contributed by stacking-faults structure shown in Figure 5B. More detailed interfacial investigation is shown in Figure 5C. The diffraction spot of $(1\bar{1}0)_{TB}$ is superimposed on the one of $(1\bar{1}0)_{L}$. It means that these two facets are coherent to each other. However, there is a rotating angle of 8° between facet $(0\bar{1}1)_{TB}$ and $(0\bar{1}1)_{L}$. It implies that a miss-conjugation happens between these two facets, and the stacking faults are introduced to the interface between them. Ultimately, it gives rise to a complete dislocation with a Burger's vector of $\vec{b}$ = $[0\bar{1}1]$ in more than 10 atomic layers of stacking-faults structure to partially release the interfacial strain. The second interface with the LAO at right also exhibits interfacial defects. The exhibition of interfacial defect is the direct evidence of strain relaxation due to the increase in NC size.

As we found in the present work, these two types of T-BFO/LAO hybrid NCs are basically controlled by their size. When the size, either BFO or LAO, is below the critical value, type 1 is formed. But when the size is larger than critical value, type 2 is formed owing to the introduction of interfacial defects in order to release the strain. The critical size boundaries for the formation of types 1 and 2 hybrid NCs are described in Figure 6 in which the phase-field approach has been employed to model the phase transition of BFO NCs as a function of BFO/LAO conjugation size.

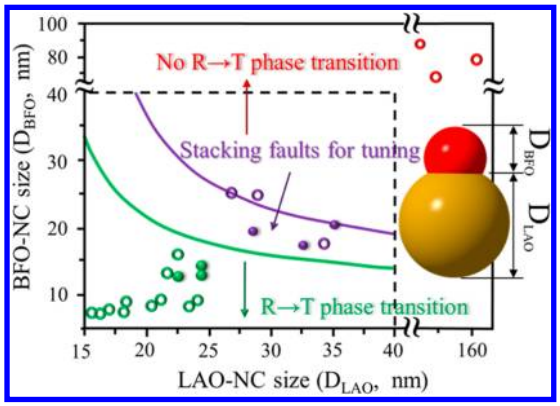

Figure 6. Effect of NC sizes, D_{BFO} and D_{LAO}, on rhombohedral-to-tetragonal (R → T) phase transition of BFO-NC. Two calculated boundary lines, green and purple, divide the phase transition area into three different zones, that is, R → T phase transition, stacking faults for tuning, and no R → T phase transition. The black-dotted line is the boundary for phase transition, that is, either BFO or LAO size locating out of line represents no phase transition taking place. Circular points represent the experimental NC sizes measured by TEM, while the solid points are the data with detailed microstructural analysis, such as the data shown from Figures 3 to 5.

Equations for Constructing NC Critical Size Boundaries. First of all, the green line in Figure 6, related to the formation of dislocation purely, was computed analytically by the following equation that determines the critical NC sizes for the dislocation emergence[29]

$$\overbrace{\left[\frac{(b_1^2+b_2^2)(J+J^*)}{2\pi}-\frac{\mu_e(1-\nu)b_3^2}{4\pi}\right]ln\left[\frac{2\pi D_{BFO}D_{LAO}}{r_0(D_{BFO}+D_{LAO})}\right]}^{Self-energy\ of\ dislocation\ array}=\underbrace{\frac{M_{BFO}M_{LAO}D_{BFO}D_{LAO}}{M_{BFO}D_{BFO}+M_{LAO}D_{LAO}}\varepsilon_m b_1}_{\substack{Interaction\ energy\ between\\ dislocation\ and\ misfit\ strain}} \quad (1)$$

in which the stored energy due to misfit strain reaches the self-energy of dislocation formation. If assuming $D_{BFO} \ll D_{LAO}$, eq 1 reduces to the classic Matthews−Blakeslee (MB) criterion.[30]

Further, as the NC size ratio (D_{BFO}/D_{LAO}) is increased beyond the critical value and more dislocations enter, the misfit strain decreases, accompanied by the retained strain partially driving the R → T phase transformation. When the dislocation space (assuming uniform distribution) is small enough (dislocation density is large enough accordingly), the relaxed

dx.doi.org/10.1021/nl500744h | Nano Lett. 2014, 14, 3314−3320

misfit strain is unable to drive the R → T phase transformation, which corresponds to the purple line in Figure 6.

Phase-field simulations integrating interfacial dislocation were performed to construct the NC size diagram (Figure 6) using the time-dependent Ginzburg−Landau (TDGL) equation

$$\frac{\partial P(x,t)}{\partial t} = -L\frac{\partial F}{\partial P(x,t)} \tag{2}$$

where L is a kinetic relaxation coefficient related to the domain wall mobility, the total free energy is F, and a function of the polarization is P, which includes all the important energetic contributions

$$F = \int_v (f_{\text{bulk}} + f_{\text{grad}} + f_{\text{elas}} + f_{\text{elec}})\mathrm{d}v \tag{3}$$

where the bulk, gradient, and electrostatic contributions are the same as those described in our previous studies.[31] In particular, the dislocations are viewed as one kind of lattice distortion and thus treated as an eigenstrain $\varepsilon_{kl}^{0,d}$, thus the elastic energy can be written in the form of

$$f_{\text{elas}} = \frac{1}{2}C_{ijkl}e_{ij}e_{kl} = \frac{1}{2}C_{ijkl}(\varepsilon_{ij} - \varepsilon_{ij}^{0})(\varepsilon_{kl} - \varepsilon_{kl}^{0}) \tag{4}$$

where C_{ijkl} is the elastic modulus tensor, which is, in general, spatially dependent, or inhomogeneous, and ε_{kl} is the total local strain.

$$\varepsilon_{kl}^{0} = \varepsilon_{kl}^{0,P} + \varepsilon_{kl}^{0,d}$$

$$\varepsilon_{kl}^{0,P} = Qi_{jkl}P_kP_l$$

where $\varepsilon_{kl}^{0,d}$ is described as a function of a BFO/LAO conjugation size,[29] as

$$\varepsilon_{kl}^{0,d} = \frac{1}{2d_0}(b_kn_l + b_in_k)\delta(x - x^d) \tag{5}$$

$$\overbrace{\left[\frac{(b_1^2+b_2^2)(J+J^*)}{2\pi} - \frac{\mu_e(1-\nu)b_3^2}{4\pi}\right]ln\left[\frac{\sinh\left(\frac{2\pi D_{BFO}D_{LAO}}{p(D_{BFO}+D_{LAO})}\right)}{\sinh\left(\frac{\pi r_0}{p}\right)}\right]}^{\text{Self-energy of dislocation array}} = \underbrace{\frac{M_{BFO}M_{LAO}D_{BFO}D_{LAO}}{M_{BFO}D_{BFO}+M_{LAO}D_{LAO}}\varepsilon_m b_1}_{\text{Interaction energy between dislocation and misfit strain}} \tag{6}$$

where n_i is the component of unit vector normal to the slip plane, b_i denotes the component of Burgers vector, d_0 is the interplanar distance of slip planes, p is the dislocation space, the radius of the dislocation core is taken as $r_0 = b/4$, and $\delta(x-x^d)$ is the Dirac delta function with x^d being a point inside dislocation loop on the slip plane. The bimaterial constants J and J^*, the effective shear modulus μ_e, as well as the biaxial modulus M_{BFO} and M_{LAO}, can be deduced from the shear modulus (μ_b and μ_l), and Poisson's ratio ν of BFO and LAO NCs. From eq 6, with given material properties the dislocation density at interface (and its resulting eigenstrain) can be tuned by varying the size of the BFO/LAO conjugation and thereby controls the R → T transition of BFO-NC. In the phase-field simulation, the shear modulus values associated with BFO and LAO NCs were used to be μ_b = 31−49 GPa and μ_l = 115.33 GPa, respectively, which stems from the first principle calculations.[32] Poisson's ratio was assumed to be the same for both NCs and set within the range of ν = 0.2−0.3. The misfit strain due to mismatch of lattice constant was employed as ε_m = 0.0447 directly obtained from our experiment. The computational approach is the same as described in our previous work on diagrams of domain stability.[31]

Figure 6 shows the results of simulation work mentioned above and experimental data of TEM investigation about the effect of NC sizes, D_{BFO} and D_{LAO}, on R → T phase transition of BFO-NC. Two calculated boundary lines, purple and green, divide the phase transition area into three different zones, that is, R → T phase transition, stacking faults for tuning, and no R → T phase transition. The black dotted line is the boundary for phase transition, that is, as long as either BFO or LAO size locating out of the boundary no phase transition takes place.

From Figure 6, when the NC sizes (either BFO or LAO-NC size) locate at the zone beneath green line, the interfacial strain between LAO-NC and BFO-NC is able to drive the R → T transition happening. As the sizes fall at the zone between green and purple lines, the hybrid NCs are becoming larger so that the stacking faults or misfit dislocations are introduced for decreasing epitaxial strain. However, the retained strain may be able to partially drive the phase transition. In other words, NC size in this zone would lead to formation of tetragonal BFO accompanying with stacking faults. Once the NC size increases beyond the threshold value above the purple line, the dislocation density will exceed the critical value, thereby eliminating the R → T transition occurrence. Lattice image of R-BFO in a heteroconjugation NC of BFO/LAO with size out of the purple line is given in the Supporting Information (Figure S4). The experimental results with different NC sizes are also plotted in the figure, where the circular points represent the experimental NC sizes measured by TEM, and the solid points stand for the data with detailed microstructural analysis. The excellent agreement between simulation and experimental results further confirms a strong relationship of hybrid size and phase transition of BFO.

To sum up, so far the design concept on the conjugation of NCs is still based on charge interaction or band engineering. Since the discovery of strain engineering, it has been widely applied to thin film for tuning physical properties of many materials, especially for complex oxides to manipulate lattice, charge, orbital, and spin degrees of freedom. A strike example for showing application of strain engineering to tune properties is the well-studied BFO system. When the applied strain reaches critical value (4−5%) by confinement of LAO substrate, BFO transforms from rhombohedral to tetragonal-like phase, and the strain leads to change in not only properties, that is, ferroelectricity and magnetism, but also phase. Owing to this feature, various potential applications such as magneto-electric effects, photovoltaic, and photocatalyst have been demonstrated. We believe that BFO-NC should be applicable to these applications. On the basis of the knowledge built up in 2D thin film, an interesting question arises: Does epitaxial strain engineering of NC possibly exist? Or more specifically, can one apply epitaxial strain to 0D NC for tuning or changing their properties? In order to demonstrate this concept, we investigated the conjugation of BFO-NC/LAO-NC since LAO is able to fully confine BFO at critical strain with suitable size. The present results show that this concept is possible to be demonstrated in NC level and to change either LAO or BFO NC size would possibly lead to tuning stability of R → T phase transition of BFO-NC. The same concept should be possibly applied in other complex oxide systems. This observation delivers a new generic approach and opens a new avenue to tailor the properties of complex oxide NCs via strain engineering or lattice interaction. This study can stimulate

dx.doi.org/10.1021/nl500744h | Nano Lett. 2014, 14, 3314−3320

further research in this direction to meet different expertise from complex oxide thin film community and NC synthesis community. More desirable functionalities of NCs can be developed based on this finding for practical applications.[33]

■ ASSOCIATED CONTENT

Supporting Information

Additional results and discussion, Figures S1−S4, and references. This material is available free of charge via the Internet at http://pubs.acs.org.

■ AUTHOR INFORMATION

Corresponding Author

*E-mail: yhc@nctu.edu.tw.

Notes

The authors declare no competing financial interest.

■ ACKNOWLEDGMENTS

This work is supported by the National Science Council, R.O.C (NSC-101-2119-M-009-003-MY2), Ministry of Education (MOE-ATU 101W961), and Center for Interdisciplinary Science of National Chiao Tung University.

■ REFERENCES

(1) Campbell, C. T. *Science* **2004**, *306*, 234−235.
(2) Pérez-Juste, J.; Pastoriza-Santos, I.; Liz-Marzán, L. M.; Mulvaney, P. *Coord. Chem. Rev.* **2005**, *249*, 1870−1901.
(3) Glotzer, S. C.; Solomon, M. J. *Nat. Mater.* **2007**, *6*, 557−562.
(4) Smith, A. M.; Nie, S. *Acc. Chem. Res.* **2010**, *43*, 190−200.
(5) Chen, W. T.; Yang, T. T.; Hsu, Y. J. *Chem. Mater.* **2008**, *20*, 7204−7206.
(6) Mannhart, J.; Schlom, D. G. *Science* **2010**, *327*, 1607−1611.
(7) Hwang, H. Y.; Iwasa, Y.; Kawasaki, M.; Keimer, B.; Nagaosa, N.; Tokura, Y. *Nat. Mater.* **2012**, *11*, 103−113.
(8) Ju, L.; Sabergharesou, T.; Stamplecoskie, K. G.; Hegde, M.; Wang, T.; Combe, N. A.; Wu, H.; Radovanovic, P. V. *J. Am. Chem. Soc.* **2012**, *134*, 1136−1146.
(9) Yamaura, K.; Huang, Q.; Zhang, L.; Takada, K.; Baba, Y.; Nagai, T.; Matsui, Y.; Kosuda, K.; Muromachi, E. T. *J. Am. Chem. Soc.* **2006**, *128*, 9448−9456.
(10) Kovalenko, M. V.; Bodnarchuk, M. I.; Lechner, R. T.; Hesser, G.; Schäffler, F.; Heiss, W. *J. Am. Chem. Soc.* **2007**, *129*, 6352−6353.
(11) Corral-Flores, V.; Bueno-Baqués, D.; Ziolo, R. F. *Acta Mater.* **2010**, *58*, 764−769.
(12) Tang, D.; Yuan, R.; Chai, Y.; An, H. *Adv. Funct. Mater.* **2007**, *17*, 976−982.
(13) Dai, Q.; Berman, D.; Virwani, K.; Frommer, J.; Jubert, P. O.; Lam, M.; Topuria, T.; Imaino, W.; Nelson, A. *Nano Lett.* **2010**, *10*, 3216−3221.
(14) Haeni, J. H.; Irvin, P.; Chang, W.; Uecker, R.; Reiche, P.; Li, Y. L.; Choudhury, S.; Tian, W.; Hawley, M. E.; Craigo, B.; Tagantsev, A. K.; Pan, X. Q.; Streiffer, S. K.; Chen, L. Q.; Kirchoefer, S. W.; Levy, J.; Schlom, D. G. *Nature* **2004**, *430*, 758−761.
(15) Biswas, A.; Rajeswari, M.; Srivastava, R. C.; Venkatesan, T.; Greene, R. L.; Lu, Q.; Lozanne, A. L.; Millis, A. J. *Phys. Rev. B* **2001**, *63*, 184424.
(16) Pesquera, D.; Barla, H. A.; Pellegrin, E.; Bondino, F.; Magnano, E.; Sánchez, F.; Fontcuberta, J. *Nat. Commun.* **2012**, *3*, 1189.
(17) Lee, J. H.; Fang, L.; Vlahos, E.; Ke, X.; Jung, Y. W.; Kourkoutis, L. F.; Kim, J.-W.; Ryan, P. J.; Heeg, T.; Roeckerath, M.; Goian, V.; Bernhagen, M.; Uecker, R.; Hammel, P. C.; Rabe, K. M.; Kamba, S.; Schubert, J.; Freeland, J. W.; Muller, D. A.; Fennie, C. J.; Schiffer, P.; Gopalan, V.; Johnston-Halperin, E.; Schlom, D. G. *Nature* **2010**, *466*, 954−959.
(18) Stranski, I. N.; Krastanow, L. *Abh. Math.-Naturwiss. Kl., Akad. Wiss. Wien* **1938**, *146*, 797−810.
(19) Chiriac, H.; Óvári, T. A.; Pop, Gh. *Phys. Rev. B* **1995**, *52*, 10104−10113.
(20) Chiriac, H.; Óvári, T. A. *J. Magn. Magn. Mater.* **2002**, *249*, 46−54.
(21) Catalan, C.; Scott, J. F. *Adv. Mater.* **2009**, *21*, 2463−2485.
(22) Zeches, R. J.; Rossell, M. D.; Zhang, J. X.; Hatt, A. J.; He, Q.; Yang, C.-H.; Kumar, A.; Wang, C. H.; Melville, A.; Adamo, C.; Sheng, G.; Chu, Y.-H.; Ihlefeld, J. F.; Erni, R.; Ederer, C.; Gopalan, V.; Chen, L. Q.; Schlom, D. G.; Spaldin, N. A.; Martin, L. W.; Ramesh, R. *Science* **2009**, *326*, 977−980.
(23) Béa, H.; Dupé, B.; Fusil, S.; Mattana, R.; Jacquet, E.; Warot-Fonrose, B.; Wilhelm, F.; Rogalev, A.; Petit, S.; Cros, V.; Anane, A.; Petroff, F.; Bouzehouane, K.; Geneste, G.; Dkhil, B.; Lisenkov, S.; Ponomareva, I.; Bellaiche, L.; Bibes, M.; Barthélémy, A. *Phys. Rev. Lett.* **2009**, *102*, 217603.
(24) Yang, J. C.; He, Q.; Suresha, S. J.; Kuo, C. Y.; Peng, C. Y.; Haislmaier, R. C.; Motyka, M. A.; Sheng, G.; Adamo, C.; Lin, H. J.; Hu, Z.; Chang, L.; Tjeng, L. H.; Arenholz, E.; Podraza, N. J.; Bernhagen, M.; Uecker, R.; Schlom, D. G.; Gopalan, V.; Chen, L. Q.; Chen, C. T.; Ramesh, R.; Chu, Y. H. *Phys. Rev. Lett.* **2012**, *109*, 247606.
(25) MacDougall, G. J.; Christen, H. M.; Siemons, W.; Biegalski, M. D.; Zarestky, J. L.; Liang, S.; Dagotto, E.; Nagler, S. E. *Phys. Rev. B* **2012**, *85*, 100406.
(26) Zhang, J. X.; He, Q.; Trassin, M.; Luo, W.; Yi, D.; Rossell, M. D.; Yu, P.; You, L.; Wang, C. H.; Kuo, C. Y.; Heron, J. T.; Hu, Z.; Zeches, R. J.; Lin, H. J.; Tanaka, A.; Chen, C. T.; Tjeng, L. H.; Chu, Y.-H.; Ramesh, R. *Phys. Rev. Lett.* **2011**, *107*, 147602.
(27) He, Q.; Chu, Y.-H.; Heron, J. T.; Yang, S. Y.; Liang, W. I.; Kuo, C. Y.; Lin, H. J.; Yu, P.; Liang, C. W.; Zeches, R. J.; Kuo, W. C.; Juang, J. Y.; Chen, C. T.; Arenholz, E.; Scholl, A.; Ramesh, R. *Nat. Commun.* **2011**, *2*, 225.
(28) Liu, H. J.; Liang, C. W.; Liang, W. I.; Chen, H. J.; Yang, J. C.; Peng, C. Y.; Wang, G. F.; Chu, F. N.; Chen, Y. C.; Lee, H. Y.; Chang, L.; Lin, S. J.; Chu, Y. H. *Phys. Rev. B* **2012**, *85*, 014104.
(29) Freund, L. B.; Nix, W. D. *Appl. Phys. Lett.* **1996**, *69*, 173−175.
(30) Matthews, J. W.; Blakeslee, A. E. *J. Cryst. Growth.* **1974**, *27*, 118−125.
(31) Chen, L. Q. *Annu. Rev. Mater. Res.* **2002**, *32*, 113−140.
(32) Shang, S. L.; Sheng, G.; Wang, Y.; Chen, L. Q.; Liu, Z. K. *Phys. Rev. B* **2009**, *80*, 052102.
(33) Suntivich, J.; May, K. J.; Gasteiger, H. A.; Goodenough, J. B.; Horn, Y. S. *Science* **2011**, *334*, 1383−1385.